Springer

Journal of
Mechanical
Science and
Technology

Journal of Mechanical Science and Technology 23 (2009) 1118~1131

www.springerlink.com/content/1738-494x
DOI 10.1007/s12206-008-1012-6

Analysis of weld-induced residual stresses and distortions in thin-walled cylinders †

Naeem Ullah Dar[1], Ejaz M. Qureshi[2,*] and M.M.I Hammouda[1]

[1]*Department of Mechanical Engineering, University of Engineering & Technology, Taxila, Pakistan*
[2]*Department of Mechanical Engineering, College of Electrical & Mechanical Engineering, National University of Sciences & Technology, Rawalpindi, Pakistan*

(Manuscript Received January 14, 2008; Revised August 10, 2008; Accepted September 26, 2008)

Abstract

Circumferential weld specifically in thin-walled structures is a common joint type in the fabrication of structural members in aerospace, aeronautical and pressure vessel industries. This type of weld joint suffers various types of weld-induced residual stress fields (hoop and axial) and deformation patterns (axial shrinkage, radial shrinkage). These imperfections have negative effects on fabrication accuracies and result in low strength welded structures that can lead to premature failures. To precisely capture the distortions and residual stresses, computational methodology based on three-dimensional finite element model for the simulation of gas tungsten arc welding in thin-walled cylinders is presented. Butt-weld geometry with single "V" for a 300 mm outer diameter cylinder of 3 mm thick is used. The complex phenomenon of arc welding is numerically solved by sequentially coupled transient, non-linear thermo-mechanical analysis. The accuracy of both the thermal and structural models is validated through experiments for temperature distribution, residual stresses and distortion. The simulated result shows close correlation with the experimental measurements.

Keywords: FE; Numerical simulations; Welding simulations; Thermo-mechanical analysis; Residual stresses; Distortions; Thin-walled cylinder; Heat source model

1. Introduction

To produce high strength welded structures, arc welding is an effective and economic joining method attracting world welding community. Due to the non-uniform expansion and contraction of the weld metal and surrounding base metal by heating and cooling cycles during welding, thermal stresses occurs in the weld and the adjacent areas. During the heating phase, the strains produced always induce plastic deformation of the metal. The stresses resulting from these strains combine and react to produce internal forces that cause a variety of welding distortions. The problem of reduced strength of the structures in and around the weld zone due to residual stresses and fitment/appearance issues due to poorly fabricated and distorted structures has been a major concern of the welding industry for decades. Circumferentially welded thin-walled cylinders are widely used in many engineering applications, including pressure vessels along with structures in aeronautical, aerospace and nuclear industries. Therefore, precise prediction of stress fields and distortion patterns (transient and residual) is of critical importance to ensure the in-service structural integrity of these welded structures.

Computer simulation tools based on numerical methods are very useful to predict welding distortions and residual stresses at the early stage of product de-

† This paper was recommended for publication in revised form by Associate Editor Dae-Eun Kim

*Corresponding author. Tel.: +92 300 500 2295, Fax.: +92 51 931 4291
E-mail address: qureshimeq@yahoo.com

sign [1, 2] along with prediction of formation of weld defects and weldability [3].

However, the complex nature of the welding process due to multi-field (thermal, mechanical, metallurgy etc.) interactions and intricate geometries in real world applications has made the prediction of weld-induced imperfections, a truly difficult and computationally intensive task. However, with the availability of 64 digit computers and refined FE tools, welding engineers around the world are more biased towards the computer simulations of complex welding phenomenon instead of the conventional trial and error approach on the shop floor. A significant simulation and experimental work focusing on circumferential welding is available in the literature [4-11]. As the computer simulation of welding processes is highly computationally intensive and large computer storage and CPU time are required, most of the previous research reduces computational power requirements by simplifying with assumptions such as rotational symmetry and lateral symmetry in numerical simulations [5-8]. These assumptions reduces the computational demand at the cost of the accuracy of the results because the model was over simplified by limiting the solution domain to only a section of the whole domain with forced symmetry assumptions which did not prevails. Further, these simplified assumptions are not capable of capturing the considerable effects of weld start/stop and weld tack modeling. In this regard an experimental work by Jonsson and Josefson [12] and some three-dimensional finite element (FE) studies [10, 11, 13]; reported deviations from rotational symmetry, especially at the beginning and end of the welding cycle for circumferential joint in welding of pipes with lateral symmetry. Later, by using a full three-dimensional model for multi-pass welding of pipes, Fricke et al. [14] concluded that residual stresses are by no means axis-symmetric.

In the present analysis, the temperature fields and consequently the weld-induced residual stress fields and distortion patterns are investigated by numerical simulations based on FEM modeling. To model the physics behind the gas tungsten arc welding (GTAW) process, a sequentially coupled, full 3D model is employed. Transient, non-linear thermal solution based on heat conduction, convective and radiative boundary conditions is solved in the first part to obtain the nodal temperature history. The temperature fields are further utilized as thermal loads in subsequent elasto-plastic structural analysis to obtain the transient and residual stress fields and distortions. The temperature-dependent thermo-physical properties such as conductivity, specific heat and density, and temperature-dependent thermal–structural properties including Young's modulus, Poisson's ratio, thermal expansion coefficient, yield strength and strain-hardening rate are used for thermal analysis and mechanical analysis, respectively. The metallurgical and mechanical consequences of phase transformation have been considered in the numerical modeling of the welding process. The properties for low carbon steel taken from [15] and shown in Fig. 1 are used in the analysis. The analysis is performed by using ANSYS®, a commercial finite element code [16] enhanced with author-written subroutines. Material properties except yield stress, which is slightly on the higher side, are utilized both for base and weld metals.

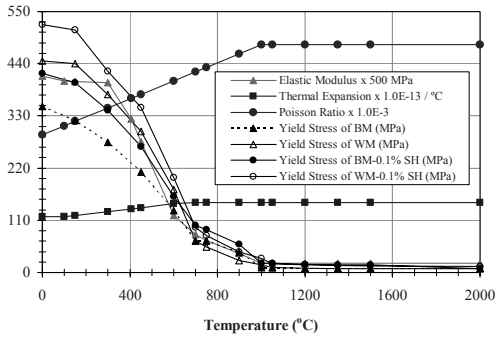

Legends : BM = Base Metal WM = Weld Metal
SH = Strain Hardening

Fig. 1. Thermo-mechanical properties of low carbon steel as a function of temperature used in the present study.

2. FE analysis

2.1 FE model

For the circumferential welding of two cylinders with "V" groove, a full 3D FE model along with finite element statistics developed in ANSYS® is shown in Fig. 2. The element type in thermal analysis is SOLID70 (linear 8-node brick element with one degree of freedom, i.e., temperature at each node) and in structural analysis is SOLID45 (linear 8-node brick element with three degrees of freedom at each node: translations in the nodal x, y, and z directions.). Further details about the selected elements may be found in [17]. High temperature and flux gradients are anticipated in and around the fusion zone (FZ) and heat affected zone (HAZ); therefore, a relatively fine mesh

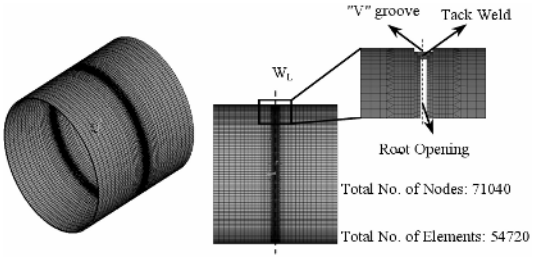

Fig. 2. (a) 3D FE mesh based on sensitivity analysis. (b) "V" groove, tack weld and root opening in FE model.

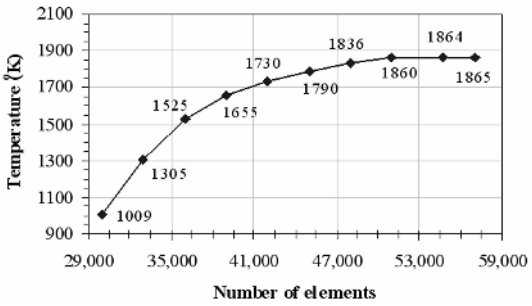

Fig. 3. Mesh sensitivity analysis based on maximum temperature attained.

is used within a distance of 10 mm on both sides of the weld line (W_L). Away from the HAZ the element size increases with an increase in the distance from W_L. In the weld direction, the element size is kept constant equal to 1.96 mm. Within the anticipated HAZ dimension of 10 mm on each side of the W_L in transverse direction, the element size of 1 mm is used.

The element size away from the weld region increases with the increase in distance. In the thickness direction there are total three elements, 1 mm each to facilitate for "V" groove modeling. Two tack welds on the start, i.e., 0º and middle, i.e., 180º of the weld are modeled, each of which is comprised of 4 elements (7.85 mm) in circumferential direction and 4 and 2 elements (4 mm and 2 mm, respectively) in two layers in the thickness direction. The used mesh is based on a mesh sensitivity analysis performed for successive mesh refinements. A number of thermal analyses based on the number of elements as indicated in Fig. 3 are conducted to see the corresponding effects of maximum temperature attained during the analysis. This maximum temperature attained is then considered as the basis for mesh refinement. As shown in Fig. 3, it is clear that no further increase in maximum temperature is achieved if the number of elements is increased beyond 54720. The mesh with number of elements indicated by the arrow in Fig. 3 is then considered for the analysis in order to get the mesh independent results. Tack lengths positions in the FE models are in accordance with the physical weld sample. Theoretically, two cylinders should be regarded as separate parts in the model setup, because they are independent until the moving heat source (welding torch) passes over and joins these together. Both the cylinders are modeled as a single model in FE modeling as the cylinders are tack welded to each other and mechanically restrained prior to welding.

2.2 Thermal analysis technique

A high non-uniform temperature field is generated during the welding process resulting in residual stresses in the welds. The transient temperature distribution is a function of total heat applied and heat distribution patterns within the domain and is highly sensitive to weld-induced residual stresses. A detailed and accurate thermal analysis with appropriate boundary conditions such as heat transfer by conduction, heat losses due to convection and radiation and heat input from the welding torch along with the effects of filler metal deposition, is of paramount importance for the determination of realistic temperature profiles. The governing equation for transient heat transfer analysis during welding process is given by Eq. (1).

$$\rho c \frac{\partial T}{\partial t}(x,y,z,t) = \nabla . q(x,y,z,t) + Q(x,y,z,t) \qquad (1)$$

where ρ is the density (kg m^{-3}) of the material, c is the specific heat capacity (J kg^{-1} K^{-1}), T is the current temperature, q is the vector of heat flux, Q is the rate of internal heat generation (W m^{-3}), t is the time (s), ∇ is the spatial gradient operator and x, y, z are the coordinates in the reference plane. The non-liner isotropic Fourier heat flux constitutive equation given by Eq. (2) is employed.

$$q = -k\nabla T \qquad (2)$$

Where k (W m^{-1} K^{-1}) is the temperature dependent thermal conductivity

The most widely acceptable double ellipsoidal heat source model, presented by Goldak et al. [18] as shown in Fig. 4, is used to present the heat generated by the welding torch for the heat input distribution to

the welds. The very small variations due to curvature of the cylinders are not taken into account. The model gives the Gaussian distribution for circumferential welding and has excellent features of power and density distribution control in the weld pool and HAZ. The spatial heat distribution in a moving frame of reference can be calculated with the governing equations Eq. (3) and Eq. (4) [18].

$$q_f = \frac{6\sqrt{3}\eta Q f_f}{\pi\sqrt{\pi}a_f bc} e^{\{-3(\frac{x^2}{a_f^2}+\frac{y^2}{b^2}+\frac{z^2}{c^2})\}} \quad (3)$$

$$q_r = \frac{6\sqrt{3}\eta Q f_r}{\pi\sqrt{\pi}a_r bc} e^{\{-3(\frac{x^2}{a_r^2}+\frac{y^2}{b^2}+\frac{z^2}{c^2})\}} \quad (4)$$

Where, $Q = VI$ and $f_f + f_r = 2$

a_f is the length of the front ellipsoidal (m)
a_r is the length of rear ellipsoidal (m)
b is the width of heat source (m)
c is the depth of heat source (m)
f_f is the fraction of heat in front ellipsoidal
f_r is the fraction of heat in rear ellipsoidal
Q is the total heat input (watts)
V is the welding voltage (volts)
I is the welding current (amperes)

The calculated volumetric heat flux densities are required to be assigned to specific elements around the welding areas in the FE model to simulate the welding torch movement with the specific welding speed. An author-written APDL subroutine is used to calculate the centroidal distance of elements from the moving arc center corresponding to the arc position at any instant by keeping the origin of the coordinate system located at the center of the moving arc. Based on the FE mesh generated by the ANSYS®, definitions of the welding process parameters and characteristics of the heat source transient heat fluxes representing the moving distributed heat source can be calculated on specific positions in welding areas. The heat source is assumed to move through volume, and calculated heat is applied to elements as volumetric heat generation so that the elements lying on the surface can be used for modeling of surface heat convection which otherwise require laying of additional two dimensional surface elements for convection modeling. The numerical values for heat source parameters used in this paper are shown in Table 1 in conjunction with the welding process parameters shown in Table 2. These parameters are calibrated through the experimental validations presented in section 3.

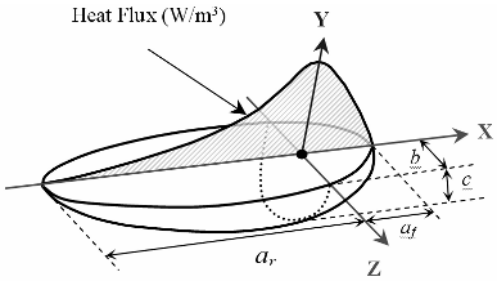

Fig. 4. Heat source model used in the present study.

A combined heat transfer coefficient for convection and radiation [19] is calculated and applied on all the exposed surfaces. The heat losses from the surfaces are modeled from the Eq. (5) and Eq. (6).

$$q_{loss} = q_{convection} + q_{radiation} \quad (5)$$

$$q_{loss} = h_{total} \text{ x } A(T - T_{amb}) \quad (6)$$

Where, A is the surface area, T is current temperature, T_{amb} is the ambient temperature and h_{total} is combined convection and radiation coefficient, given by Eq. (7).

$$h_{total} = [h + \varepsilon\sigma(T + T_{amb})(T^2 + T_{amb}{}^2)] \quad (7)$$

Where, h is the thermal convection coefficient (8 $Wm^{-2}K$ in the present study), ε is the radiation emmissivity, σ is the Stefan-Boltzmann constant (5.67 x 10^{-8} W $m^{-1}K^4$) on the surface of the steel under investigation in the present study, $\varepsilon = 0.51$ is used which is

Table 1. Numerical values of heat source parameters.

Parameter	Value
Length of front ellipsoidal, a_f (m)	0.005
Length of rear ellipsoidal, a_r (m)	0.015
Width of heat source, b (m)	0.010
Depth of heat source, c (m)	0.003
Fraction of heat in front ellipsoidal, f_f	1.25
Fraction of heat in rear ellipsoidal, f_r	0.75

Table 2. Welding process parameters.

Parameter	Value
Welding voltage [Volts]	12.5
Welding current [Amperes]	200
Welding process efficiency [%]	80
Welding Speed [mm/s]	3

the average value for hot rolled steel plates. T_{amb} is taken as 300 K equal to the room temperature. The heating time along the weld path is about 314.16 s with a torch speed 3.0 mms^{-1} and the complete welding sequence is divided into 480 incremental equally spaced load/solution steps of 0.87 s. Stepped load option available in ANSYS® is used for effective application of thermal load during the load step. After extinguishing the arc an additional 47 load steps of different lengths are used for cooling of the weldment. The total cooling time to return to the ambient temperature of 300 K is about 1500 s (25 min) from the start of the cooling phase.

A relatively straightforward and easy to implement by utilizing the ANSYS® embed features of element birth and death, conventional quite element technique [20] is used in the present work. The whole FE model is generated in the start, however; all the elements representing filler metal are deactivated by assigning them very low conductivity. During the thermal analysis, all the nodes of deactivated elements (except those shared with the base metal) are also fixed at ambient temperature till the birth of the respective element. Deactivated elements are re-activated sequentially when they come under the influence of the heat source (welding torch).

2.3 Structural analysis technique

The temperature history of each node from the preceding thermal analysis are input as nodal body load in conjunction with temperature-dependent mechanical properties and structural boundary conditions as shown in Fig. 5 in the sequel mechanical analysis.

Thermo-elastic–plastic material formulation as shown by Eq. (8) [21] with von Mises yield criteria is employed with σ_1, σ_2, and σ_3 being the three principal stresses, coupled to a kinematic hardening rule.

$$\sigma_v = \sqrt{\frac{1}{2}[(\sigma_1-\sigma_2)^2+(\sigma_2-\sigma_3)^2+(\sigma_3-\sigma_1)^2]} \qquad (8)$$

Same meshing parameters from thermal analysis to facilitate the nodal data mapping and elements with same topology to enhance the convergence during the structural analysis are used. The critical issue of element birth and death from the thermal analysis is handled by an author-written subroutine. The sequential birth of an element takes place when the element reaches the solidification temperature. Melting and ambient temperatures are set as the temperatures at

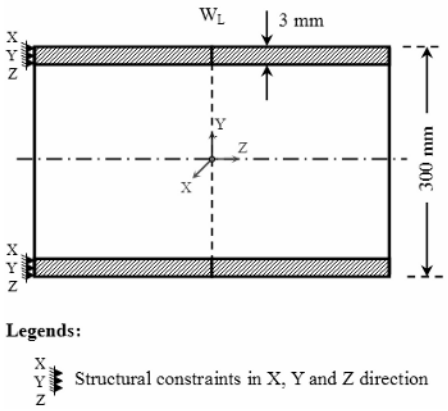

Fig. 5. Schematic representation of structural boundary conditions employed (not to scale).

which thermal strains are zero for thermal expansion coefficients of the filler and base metals.

Additionally, to handle the excessive distortion issues, initial strains in the elements are set to zero at the time of element reactivation. In structural analysis, the only boundary condition is the constraints applied to represent the clamping of the cylinders to be welded in welding positioners, i.e., all the nodes at the positioner end of the cylinders, on a Cartesian coordinate axis, are constrained in axial direction. Additionally, two nodes 180° apart at the positioner end are also constrained in axial, radial and circumferential directions for FE model stability. The other remote face of the cylinder is restraint free. During analysis (both thermal and structural), a 'Full Newton–Raphson' iterative solution technique with a direct sparse matrix solver is used for obtaining the solution. During the thermal cycle, temperature, and consequently temperature-dependent material properties, changes very rapidly; thus, a Full Newton–Raphson scheme, which uses a modified material properties table and reformulated stiffness matrix after equilibrium iterations, is believed to give more accurate results than other options such as Modified or Initial Newton–Raphson schemes. Line search option of the FE code ANSYS® is set to ON to improve convergence. The use of a single point reduced integration scheme is implemented with hourglass control to facilitate convergence and to avoid excessive locking during structural analysis is implemented.

3. Experimental verification

The appropriate way to ensure the reliability of the

numerical simulations and to extend the utilization of the research work for shop floor applications is by conducting full-scale experiments with proper instrumentation for data measurement. For arc welding experiments, automatic welding setup with minimum human intervention and skill is considered as mandatory for the proper validation of numerical results due to the variations associated with the skill of the operators and rotary synchronization problems. Similarly, the careful data acquisition during the experiments is of critical importance and demands a proper data measurement and analysis system. In the present research, to ensure the reliability of the FE models, GTAW experiments on two thin-walled cylinders with similar geometric and welding process parameters from the finite element models are conducted. Low carbon steel equivalent to AH36 with chemical composition as shown in Table 3 having slight variations in chemical composition from the material model used in the simulation is utilized. Similar approximations were made in the past by [22] with comparable measured and predicted results. In addition to the FE parameters, argon with 99.999% purity was used as shielding gas with flow rate of 15 liters/min. Commercially available high-tech, fully automatic SAF GTAW welding equipment along with rotary positioners and welding fixtures was used to reflect the desired structural boundary conditions. Single pass welding equipment along with rotary positioners and welding fixtures was used to reflect the desired structural boundary conditions. Single pass butt-weld geometry is used with single "V" groove having included angle of 90^o and 2 mm root opening as shown in Fig. 6.

The welding specimen consists of two 150 mm outer diameter and 3 mm wall thickness cylinders. Two tack welds starting from 0^o (weld start position) equally spaced at 180^o, each with length of ~ 8 mm were placed. These tack welds were also used to create a root opening prior to welding by insertion of additional spacers of 2 mm at some appropriate locations during tack welding. The spacers were removed after the tack welds were cooled to room temperature. To minimize the initial stress effects prior to welding due to tack welds, the areas in and around the tack welds were treated with post weld heating to 573K (300^oC). Conventional gas torch heating with both infrared and touch probe thermocouples measurement was utilized. However, the stress data after the tack welds and after the post weld heating was not recorded and the effects are ignored. Further, as these cylinders were linearly seam welded after roll forming of sheet metals, the effects of the linear seam weld was also not considered in this work. The furnace stress relieving prior to circumferential tack welds is a reasonable justification for not considering these effects.

Table 3. Chemical composition of low carbon steel.

% Chemical Composition			
C	0.130	V	0.056
Cr	0.026	Cu	0.015
Mn	1.418	S	0.007
Si	0.012	P	0.023
Si	0.346	Sn	0.002

The nodal temperature distributions from the thermal analysis are used as a basic input for the sequel structural analysis. Therefore, experimental data correlation for the FZ and HAZ dimensions or alternatively some nodal temperature verification for accurate predictions of subsequent stress fields and distortion patterns is a prerequisite. The latter technique by using the thermocouples and data acquisition system with computer interface is adopted for the thermal model validation in the present study. Thermocouples at four different locations were placed and temperature recorded through the data logger after every 10 seconds of time interval for comparison with FE results. A quantitative comparison of measured and predicted transient temperatures at thermocouple locations is presented in Fig. 7. The thermocouples TC1, TC2 and TC3 show close agreement with the FE data. Whereas, thermocouple TC4 shows comparatively higher variation of predicted and measured temperatures. Overall, the results are within the maximum variation of 8% and are reasonably acceptable.

Residual stresses are measured at some specified points for comparison through the predicted results

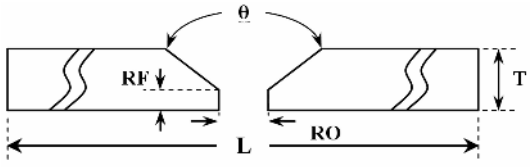

RF	θ	RO	T	L
1 mm	90°	2 mm	3 mm	300 mm

Fig. 6. Butt-weld joint geometry (not to scale).

for structural model validation. A center hole drilling strain gauge method is used to measure the residual hoop and axial stresses at specified locations, i.e., points P1 to P3 on cylinder outer surface and P4 to P6 on cylinder inner surface. Refer to the gauge location from P1 to P6 in Fig. 8. The details of the hole drilling residual strain measurement method can be found in [23]. A quantitative comparison of residual stresses from experiments with predicted data, showing good agreement, can be found in Fig. 8. From the qualitative comparison of nodal temperatures and residual stresses from Fig. 7 and Fig. 8, it is evident that predicted results agreed well with the experimental data; thus the developed models have been experimentally validated.

4. Results and discussion

4.1 Thermal analysis

Fig. 9(a-d) shows the temperature distributions for four different times during the welding process.
As anticipated, the peak temperatures are observed at the heat source location (i.e., close to W_L). Steep temperature gradients are observed ahead of the heat source, showing the least significance of heat flow ahead of the welding torch. The gradients behind the torch show the cooling phenomenon after peak temperature achieved, as the torch moves ahead from certain point. Fig. 9(d) shows the temperature distribution when the weldments are cooled to almost uniform temperature, followed by some more time steps further simulating the cooling phase.

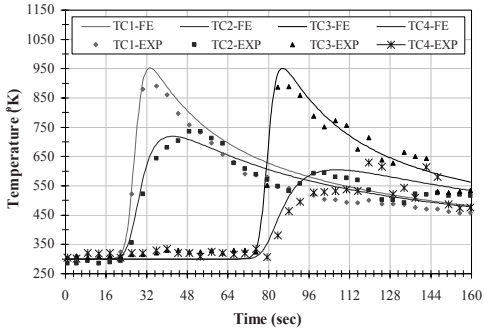

Thermocouple location	TC1	TC2	TC3	TC4
Distance from W_L (mm)	10	15	10	20
Distance from weld start (°)	30	30	90	90

Fig. 7. Comparison of computed and measured transient temperature profiles at four different locations on cylinder outer surface.

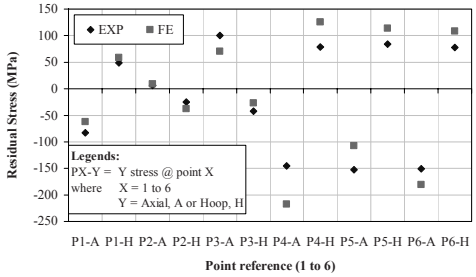

Strain gauge location	P1	P2	P3	P4	P5	P6
Distance from W_L (mm)	10	15	20	10	10	10
Angle from weld start (°)	30	30	30	45	125	225

Fig. 8. Computed and measured residual stress values for different locations at cylinder outer surface.

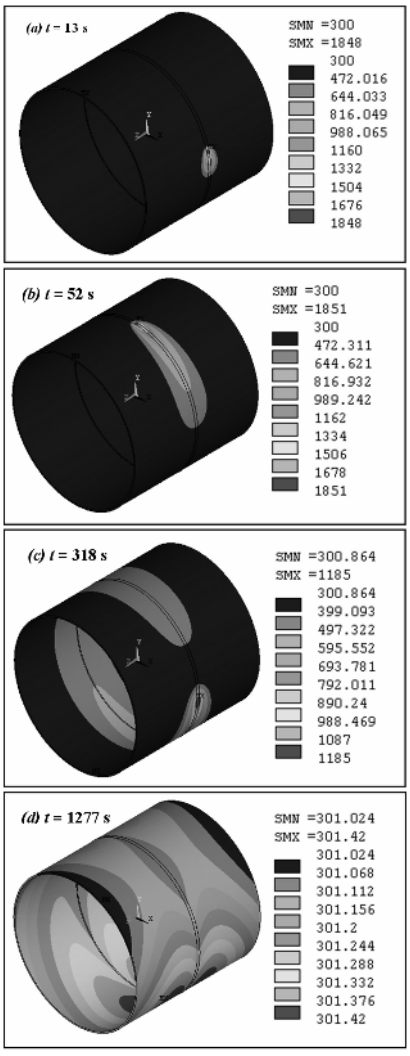

Fig. 9. Temperature profiles at four different time steps during the welding process.

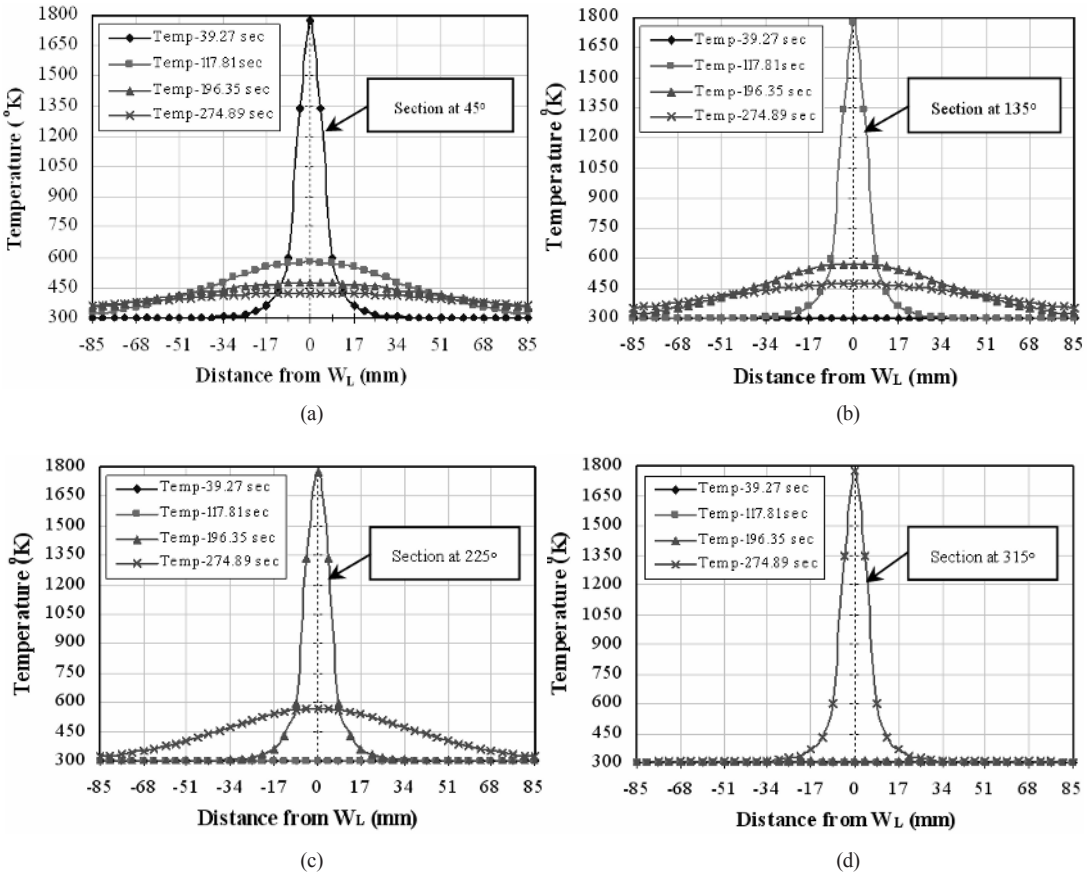

Fig. 10. Axial temperature distributions for four different cross-sections at different time steps from the weld start.

Fig. 10(a-d) shows the axial temperature distributions for different cross-sections at different time steps from the weld start towards the time progress. It is clear that the temperature distribution at a section is steep as the arc crosses the section, e.g., in case of Fig. 10(a) the section is located at an angle of 45° from the weld start position, i.e., 0°. A welding torch traveling at a speed of 3 mm/s around a circumference of 300 x π reaches the section after 39.27 s. Hence maximum temperature as expected is observed at the torch position. The temperature falls slowly as the torch crosses the section. A preheating action of the section due to the forward heat flow through the torch just before the torch arrival at a section is also shown and is more dominant in-case for the sections oriented at 225° and 315° as depicted in Fig. 10(c) and Fig. 10(d), respectively.

Fig. 11(a-d) shows the transient thermal cycles experienced by various points at 0 mm, 5 mm and 15 mm from the W_L and at 0°, 90°, 180° and 270° respectively from the weld start position. The thermal cycles shows that temperature at a point reaches a peak value corresponding to a time when the arc crosses the corresponding section. It is also evident from the figure that a point nearest to the W_L gets heated to a maximum extent, while points away from the W_L experiences peak temperatures which are exponentially lower. Fig. 12 further elaborates on the temperature distribution by using Goldak's heat source model.

4.2 Residual stress analysis

4.2.1 Axial residual stress fields

For circumferentially welded cylinders, stress normal to the direction of the weld bead is the axial stress. Compressive and tensile axial stress fields are observed in and near the weld region on the outer and inner surfaces of the cylinders, respectively. This is attributed to different temperature profiles on the inner and outer surfaces of the cylinders. Varying shrinkage patterns through the wall thickness on the

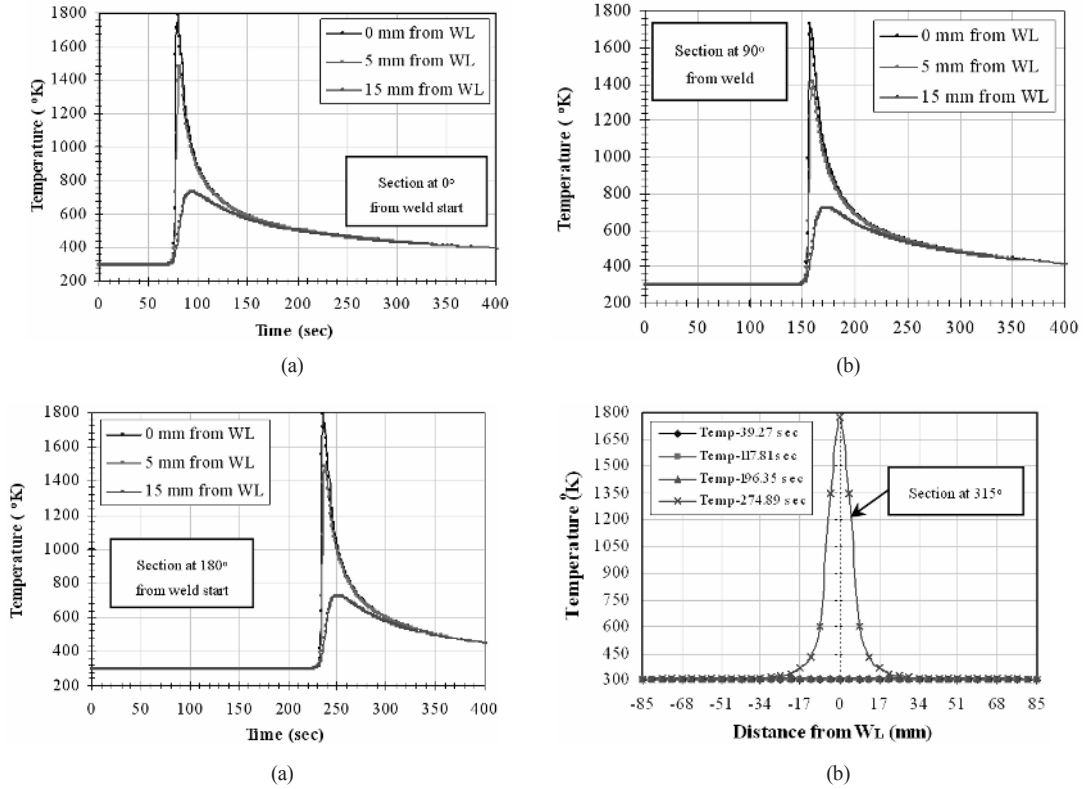

Fig. 11. Transient thermal cycles experienced by various points at different cross sections from the weld start position.

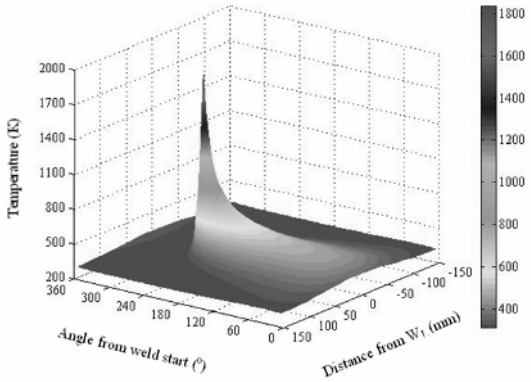

Fig. 12. Temperature contour plots.

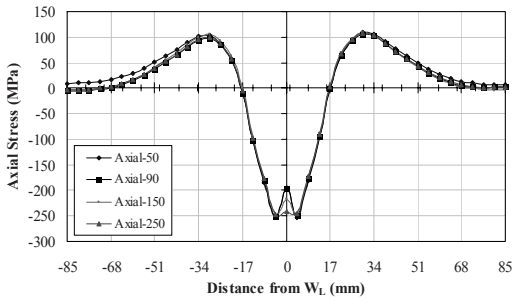

Fig. 13. Residual axial stresses (MPa) on outer surface at different cross sections from the weld start position.

inner and outer surfaces due to different temperature gradients; results in tensile and compressive residual stress fields on inner and outer surfaces, respectively, near the weld line (W_L). Fig. 13 shows axial stress distributions on the cylinder's outer surface at differ ent cross sections from the weld start position. The convention used is that Axial-50 represents the axial stress at 50° from the weld start position and so on. The compressive residual axial stresses near the W_L-diminish to zero after 17 mm on both sides of the W_L. Beyond this, a stress reversal from compressive to tensile is observed.

These low magnitude tensile stresses again approach a zero value almost 68 mm away from the W_L. After 68 mm from the W_L a constant axial stress value near to zero is obvious from Fig. 13. The high tensile stresses near the W_L approach to zero and then reverse to lower compressive residual stresses at 17 mm, again increasing to almost constant value of zero at 68 mm on both sides of W_L observed for cylinder

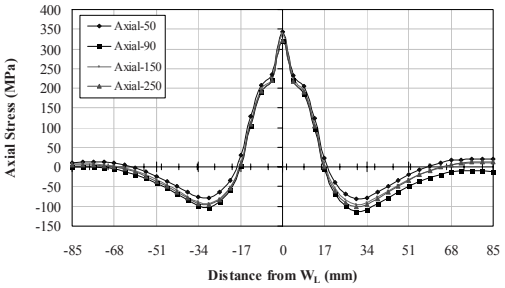

Fig. 14. Residual axial stresses (MPa) on inner surface at different cross sections from the weld start position.

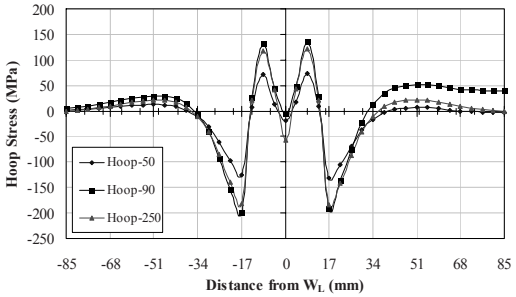

Fig. 15. Residual hoop stresses (MPa) on outer surface at different cross sections from the weld start position.

inner surfaces at different cross sections from weld start position as shown in Fig. 14.

The general residual axial stress profile shows close analogy with the previous research [5, 8, 10, 12, 13]. The variation in magnitude (higher or lower residual stresses) in the present research work is attributed to the different material properties, i.e., mechanical properties like yield strength for base and weld filler metals along with other parameters such as weld geometry and heat source parameters. Some observations of the significance pertaining to axial stress fields from Fig. 13 and Fig. 14 are as follows:

- Due to symmetry across the W_L, the stresses are also symmetric. In and around the FZ, the high magnitude stress fields, i.e., compressive and tensile for outer and inner surfaces, respectively, are observed.
- Axial stresses are weakly dependent on the circumferential location. Fig. 13 and Fig. 14 clearly reveal that axial residual stresses on outer and inner surfaces at four different cross sections (50^o, 90^o, 150^o and 250^o) are almost of the same magnitude and trend. This is in absolute agreement with the previous research [5]. Except the weld start and its vicinity, the axial stress around the circumferential direction almost has a homogeneous distribution.
- At the outer surface of cylinders near the W_L, there is a prominent bulge indicating stress variations beneath the weld crown (refer Fig. 13).

4.2.2 Hoop residual stress fields.

Stresses parallel to the direction of the weld bead are known as hoop stresses. The residual hoop stresses are developed due to the radial expansion and contraction during the heating and cooling sequence of welding process. Residual hoop stress distributions for outer and inner surfaces of cylinders along the axial directions in different cross sections from the weld start position are shown in Fig. 15 and Fig. 16, respectively. On the inner and outer surfaces, in and around the vicinity of the W_L, large tensile and compressive hoop stresses, respectively, are developed. Similar trends for stress reduction and stress reversal are observed for hoop residual stresses as for axial residual stresses. The trend for the hoop stress also agreed well with the previous research [5, 8, 10, 12, 13]. The quantitative variation is again attributed to different welding parameters, heat source parameters and material properties in the present and referred research work, respectively. Some important aspects are as follows:

- Hoop residual stresses are also symmetric due to symmetry across the W_L.
- Near the FZ high tensile stresses (130 MPa on outer and 313 MPa on inner surface) are predicted. Away from the HAZ region (about 17 mm from W_L), both on outer and inner surfaces a compressive residual stress of 200 MPa is observed.
- Hoop stresses are dependent on the circumferential location from weld start to weld end. From Fig. 15 and Fig. 16 it is obvious that hoop residual stresses on outer and inner surfaces at three different cross sections (50^o, 90^o, and 250^o) vary in magnitude, with almost similar trend. This is also in close agreement with the previous research [5].

4.2.3 Axial and hoop residual stress fields along the circumference

Comparison of axial and hoop residual stress distribution for outer and inner surfaces, on a circumferential path at the W_L is shown in Fig. 17. Again, the stress profiles are generally in agreement with the previous research. Some important observations are:

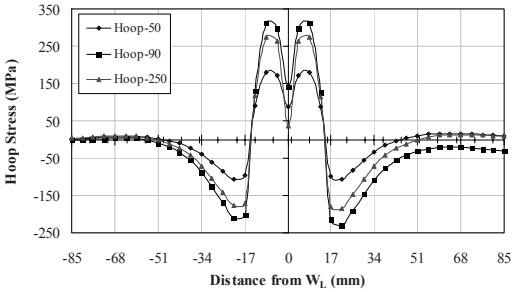

Fig. 16. Residual hoop stresses (MPa) on inner surface at different cross sections from the weld start position.

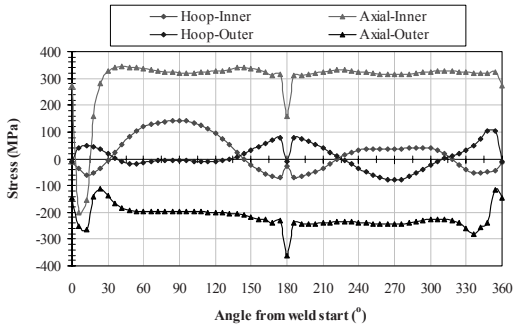

Fig. 17. Axial and hoop residual stress fields on cylinder outer and inner surfaces on a circumferential path at the W_L.

- On the outer surface, the low magnitude hoop stress (-76 MPa to 77 MPa) remains almost constant. Some exceptions at weld start/end and tack weld locations (0^o and 180^o) are observed. At these locations, almost a zero hoop stress is observed. Slight variation in magnitude and trend is observed for hoop stresses on the inner surface. The stress varies from -70 MPa to 140 MPa, with some exceptions on weld start/end and tack weld locations. Again, at tack weld locations, stress values close to zero are observed.
- On the outer surface, a compressive axial stress profile is shown in Fig. 17. The compressive stress varies from 114 MPa to 361 MPa. A low magnitude, stable stress profile from weld start to weld end with some exceptions in and in vicinity of weld start/end and tack locations is observed. The significant effects of weld start are observed for axial stress on inner surface. Also at tack weld points, the effect is prominent. The stress varies from -200 MPa to about 340 MPa in magnitude. A dip of about 472 MPa and 150 MPa is shown at the weld start of 0^o and tack weld locations of 180^o respectively.

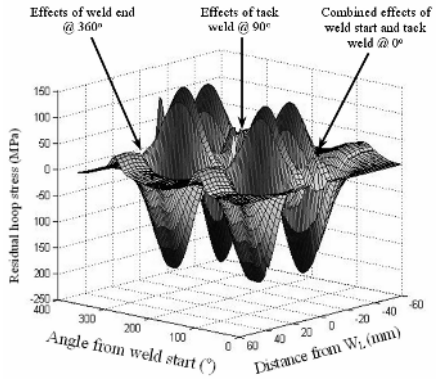

Fig. 18. Hoop residual stress fields on cylinder outer surface.

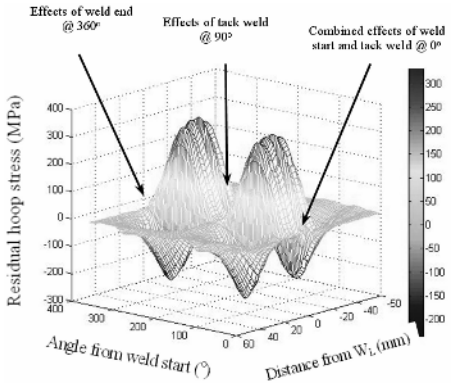

Fig. 19. Hoop residual stress fields on cylinder inner surface.

4.2.4 Stress contour plots

From previous discussion it is evident that due to weld start/end and tack welds, the residual stress varies significantly along the entire periphery. Fig. 13 and Fig. 14 for cylinder outer and inner surfaces, respectively, presents axial residual stresses at four different cross sections from weld start position at 0^o. No presentable variation is observed because the data shown is away from the weld start/end and tack weld orientations. Similarly, slight variation in hoop residual stress patterns is observed from Fig. 15 and Fig. 16 for outer and inner surfaces, respectively. Again, the data at weld start/end and tack weld location(s) is missing in this case. In order to get a better insight of the stress variation along the hoop co-ordinates, hoop residual stress fields on outer and inner surfaces are shown in Fig. 18 and Fig. 19, respectively.

From Fig. 18, on outer surfaces the stress pattern on the whole periphery is strongly affected by the weld start/end and tack weld at 180^o. Highly fluctuating stress patterns along the entire periphery, transverse to weld direction (axial direction) are obtained. Pro-

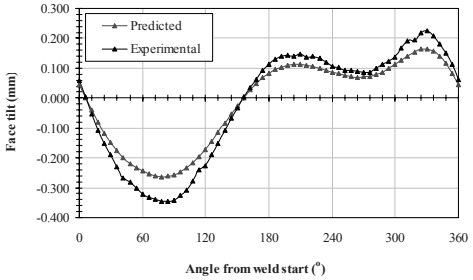

Fig. 20. Measured and predicted axial deformation (face tilt) of the cylinder face.

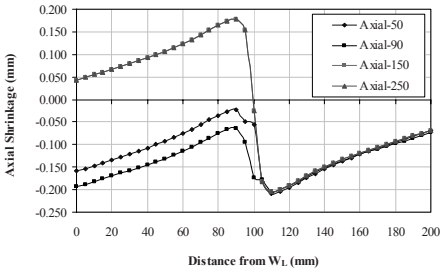

Fig. 21. Axial shrinkage at four different sections from the W_L on cylinder outer surface.

nounced localized stress reduction in and around the weld start/end and tack weld locations is shown. However, these effects are slightly less significant at the weld end location. Transverse to weld direction and away from the weld line, stress reversal is shown along the entire periphery with some exceptions at weld start/end and tack weld positions. Hoop residual stress fields from Fig. 19 on inner surface reveals that the effects of weld start and weld end are not as much pronounced as for the cylinder outer surface. However, the effects of tack weld location at 90° are quite significant. Over the entire periphery from weld start at 0° to weld end at 360°, hoop residual stress oscillates significantly in the transverse direction on both sides of the weld line. Away from the weld, the fluctuation trend is progressively stabilized.

4.3 Distortion analysis

4.3.1 Axial and radial deflection

Fig. 20 present the comparative (predicted and experimentally measured) axial tilt of the restraint-free face of the cylinder after the cooling of the weldments. Keeping in view the thickness of the cylinder face, it was difficult to accurately measure the face tilt of the cylinder experimentally.

With some appropriate arrangements and welded cylinders still in the welding positioner, a digital dial indicator was precisely positioned at an average diameter of the cylinder (in this case 297 mm) and the data was recorded by rotating the positioner. To minimize the data acquisition error, five different readings after the tack weld and after cooling of the weldments to room temperature were taken. An average value is plotted in Fig. 20 for comparison with predicted results. Axial face tilt ranging from -0.34mm to +0.23mm is observed, as the dial indicator tracks the face from 0° to 360°. The extent of axial shrinkage is dependent on a number of factors includeing welding process parameters, tack weld dimensions and orientation. For the welding process parameters and tack weld geometry in the present research, the axial shrinkage is maximum (0.263 mm) at 78° and axial deflection is maximum (0.162 mm) at 330° near the weld end. From weld start position at 0º to 150º the FE results are under predicted as compared to experimental data, from 17% to 44% with an average under prediction of 24%. From 132º to 359º again low predicted results are observed with variation of 45% to 57% at an average under prediction of 45%. Although the variation is a bit on the larger side, the results are in good qualitative agreement from weld start to weld end.

Fig. 21 shows the variability in axial shrinkage at four different sections from the W_L, at cylinder outer surface. As the coordinate axis is located on the W_L (refer Fig. 5), the shrinkage on the restraint-free end is shown to be positive. Near the W_L (10 mm from weld line towards free restraint free end), maximum axial shrinkage of 0.17 mm is indicated for axial sections at 50° and 150° from the weld start position. The axial shrinkage decreases away from the W_L towards the free end to a minimum value of 0.05 mm. Similarly, on the constrained end, a maximum axial shrinkage of 0.2 mm is observed at a distance of ~10 mm from W_L for all the sections under investigation. The axial shrinkage decreases continuously away from the W_L and a minimum shrinkage of almost zero is shown at the restrained end.

5. Conclusions

Computational methodology and techniques based on finite element analysis for the prediction of temperature profiles and subsequent weld-induced residual stress fields and distortion patterns in GTA welded thin-walled cylinders of low carbon steel are developed and implemented successfully with close correlation to the experimental investigations. De-

tailed results and discussion pertaining to residual stress fields are presented. Further, the author's also present some data pertaining to residual deformations. The following are the significant conclusions from the results presented.

(1) Along and near the weld line, a high tensile and compressive axial residual stresses occurs on the cylinder inner and outer surfaces, respectively. Compressive and tensile axial residual stresses are produced on inner and outer surfaces away from the weld line. Axial stresses are weakly dependent on the circumferential locations from weld start. With some exceptions on weld start and its vicinity, the axial stress along the circumferential direction almost has homogeneous distributions. Further, on the outer surface near the weld line, a prominent bulge indicates stress variation beneath the weld crown.

(2) Hoop residual stresses are sensitive to the angular location from the weld start position. From Fig. 15 and Fig. 16 it is evident that hoop residual stresses on outer and inner surfaces at three different cross sections vary significantly in magnitude. Further, the stress contour plots in Fig. 18 and Fig. 19 also shows significant variation of residual hoop stresses at angular locations with reference to weld start position.

(3) On the inner surface, the weld start effect is more severe for both axial and hoop stresses and is dominant in the weld start direction. A significant effect of tacks on the axial stress on the inner surface is observed at angular positions of 0° and 180° from the weld start point, whereas the effect of tacks on hoop stresses is not as prominent. The author has concluded that the stress distribution is no more axis-symmetric for a single pass butt circumferential weld with initial tacks. However, if the weld start/end effects are ignored, hoop stresses are almost uniform.

(4) Maximum axial and radial deflection is observed near the weld line. The axial shrinkage decreases continuously away from the W_L and a minimum shrinkage of almost zero is shown at the restrained end. However, on the restraint-free end some deflection (face tilt) is observed.

Acknowledgment

The authors are highly indebted to the University of Engineering & Technology (UET) Taxila, National University of Sciences and Technology (NUST) and Higher Education Commission (HEC) of Pakistan for the support provided for the research work.

References

[1] P. H. Chang and T. L. Teng, Numerical and experimental investigation on the residual stresses of the butt-welded joints, *Journal of Computational Material Science,* 29 (4) (2004) 511-522.

[2] A. Bachorski, M. J. Painter, A. J. Smailes and M.A. Wahab, Finite element prediction of distortion during gas metal arc welding using the shrinkage volume approach, *Journal of Materials Processing Technology,* 92-93 (1999) 405-409.

[3] D. Dye, O. Hunziker and R. C. Reed, Numerical analysis of the weldability of superalloys, *Acta Materialia,* 49 (4) (2001) 683-697.

[4] A. Yaghia, T. H. Hydea, A. A. Becker, W. Suna and J. A. Williams, Residual stress simulation in thin and thick-walled stainless steel pipe welds including pipe diameter effects, *International Journal of Pressure Vessels and Piping,* 83 (11-12) (2006) 864-874.

[5] D. Deng and H. Murakawa, Numerical simulation of temperature field and residual stress in multi-pass welds in stainless steel pipe and comparison with experimental measurements, *Computational Material Science,* 37 (3) (2006) 269-277.

[6] B. Brickstad and B. L. Josefson, A parametric study of residual stresses in multi-pass butt-welded stainless steel pipes, *International Journal of Pressure Vessels and Piping,* 75 (1) (1998) 11-25.

[7] E. F. Rybicki, D. W. Schmueser, R. W. Stonesifer, J. J. Groom and H. W. Mishaler, A Finite Element model for residual stresses and deflections in girth-butt welded pipes, *ASME Journal of Pressure Vessel Technology,* 100 (1978) 256-262.

[8] E. F. Rybicki, P. A. McGuire, E. Merrick and J. Wert, The effect of Pipe thickness on residual stresses due to girth welds. *ASME Journal of Pressure Vessel Technology,* 104 (1982) 204-209.

[9] E. F. Rybicki and R. B. Stonesifer, Computation of residual stresses due to multi-pass welds in piping system. *ASME Journal of Pressure Vessel Technology,* 101 (1979) 49-54.

[10] Y. Dong, J. Hong, C. Tsai and P. Dong. Finite Element modeling of residual stresses in austenitic stainless steel pipe girth welds, *Welding Journal, Weld Research Supplement,* 442 (1997) 449-444.

[11] R. I. Karlsson and B. L. Josefson, Three-dimensional Finite Element analysis of temperature and stresses in single-pass butt-welded pipe. *ASME Journal of Pressure Vessel Technology,* 112 (1990) 76-84.

[12] M. Jonsson and B. L. Josefson, Experimentally determined transient and residual stresses in the butt-welded pipes, *Journal of Strain Analysis,* 23 (1) (1988) 25-31.
[13] L. Karlsson, M. Jonsson, L. E. Lindgren, M. Näss-tröm and L. Troive, Residual stresses and deformations in a welded thin-walled pipe, *Proc. ASME Pressure Vessel and Piping Conf. (Hawaii, July 1989)* PVP-173 (1989) 7-11.
[14] S. Fricke, E. Keim and J. Schmidt, Numerical weld modeling-a method for calculating weld-induced residual stresses, *Nuclear Engineering and Design,* 206 (2-3) (2001) 139-150.
[15] Q. Xinhai, Numerical simulation of buckling in thin panels, *PhD Thesis, University of Carolina.* (2003).
[16] ANSYS 10.0 by ANSYS, Inc.
[17] ANSYS-10.0 user manual.
[18] J. Goldak, A. Chakravarti and M. Bibby, A new Finite Element model for welding heat source. *Metallurgical Transactions B*. 15B (1984) 299-305.
[19] I. F. Z. Fanous, M. Y. A. Younan and A. S. Wifi, Study of the effect of boundary conditions on residual stresses in welding using element birth and element movement techniques, *ASME Journal of Pressure Vessel Technology,* 125 (4) (2003) 432-439.
[20] L. E. Lindgren and R. Hedblom, Modeling of addition of filler material in large deformation analysis of multi-pass welding, *Communication in Numerical Methods in Engineering,* 17 (9) (2001) 647-657.
[21] S. A. Tsirkas, P. Papanikos and T. Kermanidis, Numerical simulation of the laser welding process in butt-joint specimens, *Journal of Material Processing Technology,* 134 (1) (2003) 59-69.
[22] L. F. Anderson, Residual stresses and deformations in steel structures, *PhD. Thesis, Technical University of Denmark,* (2000).
[23] Vishay Group, Measurement of residual stresses by the hole drilling strain gage method, *Technical Note No.TN-503*. (www.vishay.com/brands/measurements_group/guide/tn/tn503/503index.htm).

Naeem Ullah Dar received the B.Sc. and M.S. degrees in mechanical engineering from the Univer-sity of Engineering & Technology, Taxila, in 1989 and 2004 respectively. Presently, he is PhD scholar in mechanical engineering at UET, Taxila. His publications are over 25 in different Int. journals and conferences. His research includes manufacturing process (GTAW welding process, HSM process, abrasive water-jet process, incremental forming etc), welding simulations, optimization, and expert system. He spent more than 16 years in different mechanical manufacturing fields. He also received MBA degree in project management and six sigma black belt from SQII in 2005.

Ejaz M. Qureshi is currently a graduate student working for his PhD in computational weld mechanics at National University of Sciences and Technology (Pakistan). After receiving his B.S. degree in Mechanical Engineering in 1997, he worked for five years in an industrial manufacturing setup producing hi-tech welded structures. Qureshi has published numerous technical papers in professional refereed journals and conferences of international repute. He has also been an active referee for several conferences and journals. His current research interests include: manufacturing processes simulation, structural integrity of welded structures and computational plasticity of cylinders/pressure vessels.

M.M.I. Hammouda received the B.Sc. and M.Sc. degrees in mechanical engineering from Al Azhar University, Cairo, Egypt in 1970 and 1975 respectively. He received his PhD degree in mechanical engineering from Cambridge University, England in 1978. His has more than 35 publications in different International journals and conferences. The research includes mechanical behavior of engineering materials, linear elastic and elastic-plastic fracture mechanics, manufacturing process modeling and simulations. Presently being a foreign faculty professor in mechanical engineering department of UET, Taxila, Pakistan, he spent more than 25 years in academic and teaching. He is a member of the Editorial Board of the International Journal of Fatigue and Fracture of Engineering Materials and Structures. [www.blackwell-science.com].